Journal of
Ceramic Science
and Technology

J. Ceram. Sci. Technol., **09** [1] 53-60 (2018)
DOI: 10.4416/JCST2017-00066
available online at: http://www.ceramic-science.com
© 2018 Göller Verlag

Controlled Preparation of Red-Light-Emitting $(Y_{0.95}Eu_{0.05})_2O_3$ Phosphors and Vacuum Sintering of Transparent $(Y_{0.95}Eu_{0.05})_2O_3$ Ceramics

B. Lu*[1, 2, 3], H.M. Cheng[1, 2, 3], Z.G. Sun[4], L. Wang[4], J.G. Pan[1, 2, 3], H.B. Chen[1, 2, 3]

[1]Faculty of Materials Science and Chemical Engineering, Ningbo University, Ningbo 315211, China
[2]Key Laboratory of Photoelectric Materials and Devices of Zhejiang Province, Ningbo 315211, China
[3]State Key Laboratory Base of Novel Functional Materials and Preparation Science, Ningbo 315211, China
[4]Beijing Hamamatsu Photonics Technology Co., Ltd, Langfang 065001, China

received August 2, 2017; received in revised form October 13, 2017; accepted November 8, 2017

Abstract

A facile co-precipitation technique was employed for preparing well-dispersed $(Y_{0.95}Eu_{0.05})_2O_3$ phosphors using ammonium hydrogen carbonate (AHC) as the precipitant, followed by vacuum sintering at the relatively low temperature of 1700 °C for 4 h to produce transparent $(Y_{0.95}Eu_{0.05})_2O_3$ ceramics. The transparent $(Y_{0.95}Eu_{0.05})_2O_3$ ceramic, with fine grain sizes of 12 – 14 μm, has a substantially smaller bandgap (~ 4.45 eV) than the corresponding phosphor. Both the oxide powder and the transparent ceramic exhibit the typical $^5D_0 \rightarrow {}^7F_2$ transition at ~ 613 nm, corresponding to the Eu^{3+} emission upon UV excitation into the charge transfer (CT) band arising from the electronic transition from the 2*p* orbital of O^{2-} to the 4*f* orbital of Eu^{3+}. The light output of the sintered bodies can be significantly improved with heat treatment, which results in much higher outputs compared with commercial single-crystal $CdWO_4$. High-temperature densification and post-annealing processes significantly improved the photoluminescence/photoluminescence excitation (PL/PLE) intensities and external quantum efficiencies, and also led to shorter fluorescence lifetimes of the samples.

Keywords: Transparent ceramics, phosphor, yttria, optical property, Eu^{3+} doping

I. Introduction

Eu^{3+}, as one of the key rare earth activators, exhibits the red-emission band of the trivalent oxidation state at ~ 613 nm, with a highly photopic response of ~ 44 % [1–4]. Eu^{3+} activator ions have been incorporated in many host crystals for developing red-light-emitting phosphors. Eu^{3+}-activated Y_2O_3 is a well-known phosphor, which displays characteristic red emission upon UV excitation into the charge transfer (CT) band, and is extensively applied in various lighting and display systems such as fluorescent lamps, white-light-emitting diode (LED) devices, field emission displays, high-resolution X-ray imaging detectors, plasma display panels, flat-panel displays, cathode-ray tubes, and scintillation fields [5–8].

A phosphor powder can be densified into a fully dense ceramic phosphor by means of advanced powder processing and sintering techniques. Unlike the conventional powder phosphor, the favorable heat resistance of ceramic phosphors allows their use in LED devices without the organic resin that may cause degradation of luminous intensity and changes in emission color upon long-term operation [9, 10]. Therefore, ceramic phosphors represent a promising potential alternative to powder phosphors for improving the performance of white-LED devices.

* Corresponding author: lvbin@nbu.edu.cn

A cost-effective pressureless sintering technique (vacuum/atmosphere-controlled sintering) is frequently employed for the fabrication of transparent ceramics, but requires readily sinterable starting powders. Y_2O_3-based phosphor powders have frequently been prepared with various approaches such as sol-gel processing [11, 12], hydrothermal synthesis [13–15], co-precipitation [16–19], homogeneous precipitation [20–23], solid-state reactions [24, 25], and laser ablation [26]. Among these approaches, ammonium hydrogen carbonate (AHC) has been demonstrated to be an effective precipitant in wet-chemical routes for preparing readily sinterable oxide particles, which can be used to produce transparent ceramics via pressureless sintering [27–31]. In addition, the AHC precipitation route is relatively time-efficient, cost-effective, and simple to operate. The purpose of this work is to produce transparent Y_2O_3:Eu ceramics by means of vacuum sintering, using readily sinterable oxide phosphors derived from high-performance precursors via control of the AHC precipitation process and thermal decomposition.

II. Experimental Procedure

The starting materials were commercial $Y(NO_3)_3 \cdot 6H_2O$ (> 99.99 % pure) and $Eu(NO_3)_3 \cdot 6H_2O$ (> 99.95 % pure), both obtained from Kanto Chemical (Tokyo, Japan). The

mother liquor was prepared by dissolving the above nitrate salts into distilled water with the molar ratio of Eu^{3+} to total cations fixed at 5 at%, because above this concentration Y_2O_3:Eu would exhibit luminescence quenching [32–34] The $(Y_{0.95}Eu_{0.05})_2O_3$ precursor was precipitated at room temperature by dripping 1.5 M AHC (ultra-high-purity, Kanto Chemical) into 0.3 M mother liquor at a rate of ~5 mL/min under mild stirring, with the AHC/total cations molar ratio (R) varied between 2 and 4. The resultant suspension was aged for different time periods under magnetic stirring. The precipitate cake was then filtered and rinsed with distilled water and anhydrous alcohol, followed by drying at 80 °C. The dried precursor was calcined in a tube furnace under flowing oxygen gas (300 mL/min) at 1100 °C for 4 h and with a heating rate of 5 K/min, to produce an oxide powder.

The oxide powders were pre-pressed in a stainless-steel mold under a pressure of ~50 MPa and then cold isostatically pressed at ~400 MPa. The green bodies were sintered in a high-temperature tungsten heater furnace (ZW-25–20, Shanghai Chen Hua Technology Co., Ltd., China) at 1700 °C for 4 h with a heating rate of 8 K/min, under a vacuum of 10^{-3}–10^{-4} Pa. The densities of the sintered bodies were determined with the Archimedes method. The sintered ceramics were double-side ground and polished to a thickness of ~1 mm, and then annealed in an oxygen atmosphere at 1100 °C for 5 h to remove the oxygen vacancy mainly caused by the vacuum sintering.

The precursors and their oxides were characterized by means of X-ray diffraction (XRD; RINT2200, Rigaku, Japan) and field-emission scanning electron microscopy (FE-SEM; S-5000, Hitachi, Tokyo, Japan). The in-line transmittance of the ceramics was measured using an UV-Vis-near-infrared (NIR) spectrophotometer (SolidSpec-3700DUV, Shimadzu, Kyoto, Japan) in the wavelength region of 200–2000 nm. The microstructure of the samples was inspected with FE-SEM (S-4800, Hitachi, Tokyo, Japan). Statistical grain sizes of the ceramics were derived from at least 200 grains with WinRoof image analysis software and the dihedral angles were measured by means of interferometry on thermally grooved grain boundaries. The light intensity output was measured with a charge-coupled device (Hamamatsu Photonics Co., Ltd., Japan; 90 kV, 2 mA, tungsten anticathode target, self-assembly) and using a commercial $CdWO_4$ single crystal provided by Beijing Hamamatsu Photonics Technology Co., Ltd., China as a reference material. The Photoluminescence (PL) and photoluminescence excitation (PLE) spectra of the samples were measured using fluorescence spectroscopy (FP-6500, JASCO, Tokyo, Japan) at room temperature. The PL spectra were acquired upon excitations at the peak wavelengths of the CT bands, whereas the PLE spectra were obtained by monitoring the 613 nm emissions of Eu^{3+}.

III. Results and Discussion

Fig. 1 shows micrographs of the $(Y_{0.95}Eu_{0.05})_2O_3$ precursors. The R value significantly affects the morphologies of the as-obtained precursors in the liquid phase. The precursor prepared with $R = 4$ and an aging time of 1 d exhibits a two-dimensional (2D) plate-like shape with a relatively uniform thickness of ~112 nm, whereas the lateral size is irregular (Fig. 1a). Keeping the aging time constant, decreasing R to 3 leads to a hollow-structured precursor with fine particle size (Fig. 1b). This morphological feature of the precursor is different from that reported in our previous study [18], owing to the different synthesis conditions. In particular, the concentration of mother liquor selected in this work (0.3 M) is twice that adopted in the previous work (0.15 M), leading to a relatively high degree of Ln^{3+} hydrolysis (Ln = Y and Eu). The Ln^{3+} ions are hydrated to $[Ln(H_2O)_6]^{3+}$ in aqueous solution, and their hydrolysis yields six-coordinate $[Ln(OH)_x(H_2O)_{(6-x)}]^{3-x}$ species (according to Eqs. (1) and (2)). A high degree of hydrolysis of Ln^{3+}, however, induces a much lower pH in the nitrate solution (Eq. (2)). Therefore, the subsequent addition of AHC induces the release of tiny CO_2 bubbles in the reaction system (Eq. (3)), some of which provide crystal nuclei promoting the formation of the hollow structure. When R is further decreased to 2, the precursor powder displays nanosheet morphology with an average thickness of ~31 nm (Fig. 1c). Increasing the aging time up to 2 d while keeping $R = 2$ does not significantly affect the shape of the precursor, which, however, assumes a looser structure (Fig. 1d).

$$Ln^{3+} + 6H_2O \rightarrow [Ln(H_2O)_6]^{3+} \quad (1)$$

$$[Ln(H_2O)_6]^{3+} + xH_2O \rightarrow [Ln(OH)_x(H_2O)_{6-x}]^{3-x} + xH_3O^+ \quad (2)$$

$$H_3O^+ + HCO^-_3 \rightarrow CO_2 + 2H_2O \quad (3)$$

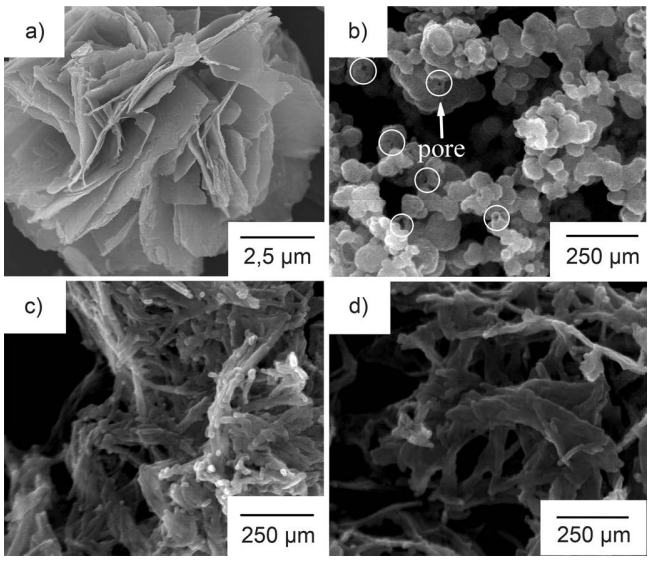

Fig. 1: FE-SEM micrographs showing the morphologies of $(Y_{0.95}Eu_{0.05})_2O_3$ precursors synthesized at $R = 4$ with 1 d aging (a), $R = 3$ with 1 d aging (b), $R = 2$ with 1 d aging (c), and $R = 2$ with 2 d aging (d).

Fig. 2 shows the morphologies of the oxide particles calcined at 1100 °C for 4 h. The $R = 4$ oxide sample retains its plate-like shape (Fig. 2a), because the thick plates are difficult to break via single-step calcination. However, after thermal decomposition both the hollow and nanosheet precursors collapse into much finer oxide powders with smooth particle edges, uniform size, good dispersion, and round particle shape (Figs. 2b–d).

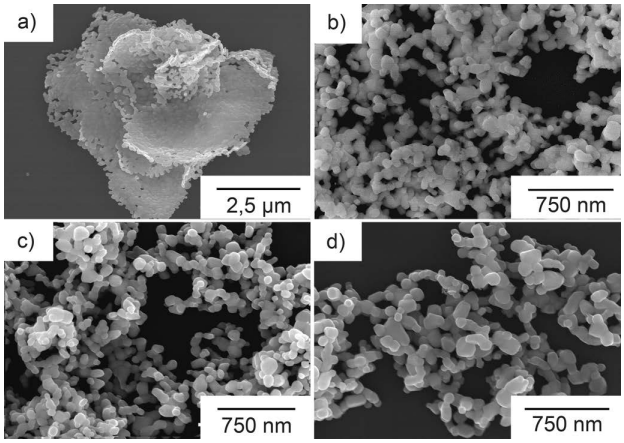

Fig. 2: FE-SEM morphologies of $(Y_{0.95}Eu_{0.05})_2O_3$ powders calcined at 1100 °C for 4 h, obtained from the precursors prepared with R = 4 and 1 d aging (a), R = 3 and 1 d aging (b), R = 2 and 1 d aging (c), and R = 2 and 2 d aging (d).

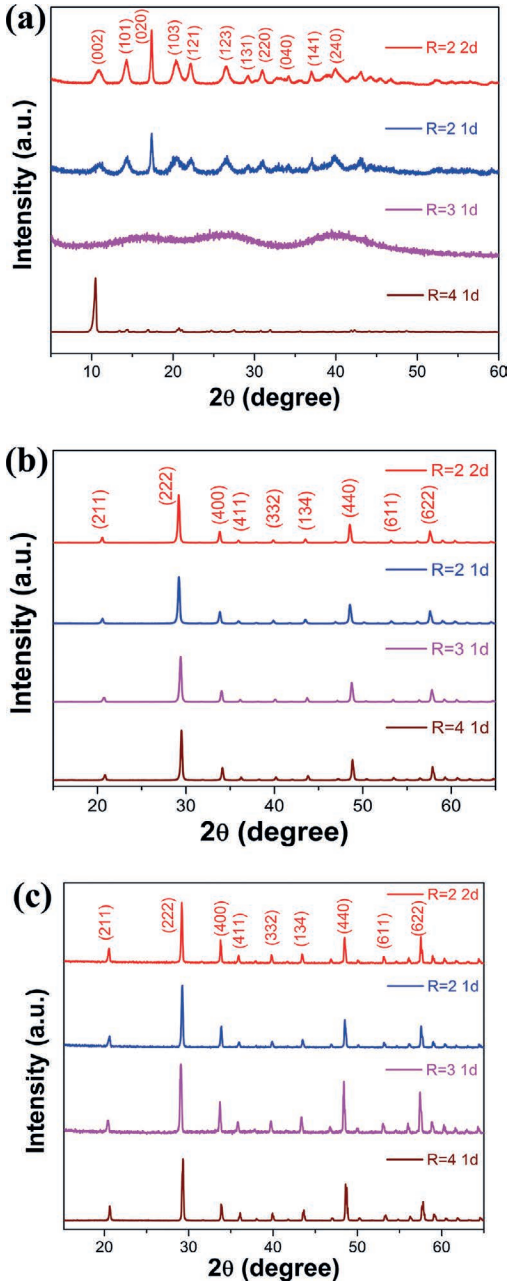

Fig. 3: XRD patterns of the Y_2O_3:Eu precursors synthesized at R = 2–4 with an aging time of 1–2 d (a), their calcination products (b) and sintered bodies (c).

Fig. 3a shows the effects of the R parameter and the aging time on the structure of the precursors. The sharp diffraction peaks of the precursor powder prepared with R = 4 denote its high crystallinity. Although the diffraction pattern could not be matched to any rare earth compound of known chemical composition, the 2D plate-like particles have structural features typical of layered rare earth carbonates, which are built by stacking the main lanthanide carbonate layer and an interlayer of water molecules [35]. The precursor powder obtained with R = 3 exhibits an amorphous phase corresponding to the spherical particle shape (Fig. 1b). As R decreases to 2, the precursor displays diffraction peaks corresponding to hydrated yttrium carbonate with orthorhombic structure (JCPDS No. 81–1538). Longer aging times, up to 2 d, further improve the crystallinity of the precursor. After calcination at 1100 °C for 4 h, all diffraction peaks of the samples can be well indexed to cubic Y_2O_3 (JCPDS No. 01–083–0927), indicating that the precursors have been converted to oxides via thermal decomposition (Fig. 3b). The as-sintered ceramics retain the cubic structure (Fig. 3c), since the phase transformation temperature of Y_2O_3 is much higher than the sintering temperature, i.e. 2308 °C for the fluorite structure and 2325 °C for the hexagonal phase [36]. However, the crystallinity of the samples was further improved at the higher sintering temperature of 1700 °C.

After compaction and vacuum sintering, the $(Y_{0.95}Eu_{0.05})_2O_3$ oxide powder made from the R = 4 precursor could not be successfully densified into a transparent ceramic, since the thick plates have low sinterability. On the other hand, transparent $(Y_{0.95}Eu_{0.05})_2O_3$ ceramics could be fabricated under further optimized synthetic conditions, involving a low R of 2–3 and aging times of 1–2 d (Fig. 4a). The absorption bands in the transmittance curve correspond to the $f \rightarrow f$ transitions of Eu^{3+} ions, and the starting wavelength of the transmittance curve was observed at ~273 nm for all ceramics. The in-line transmittances at the Eu^{3+} emission wavelength (613 nm) were 22.8 %, 30.5 %, and 60.9 % for the sintered bodies corresponding to the specimens prepared at R = 3 with 1 d aging, R = 2 with 1 d aging, and R = 2 with 2 d aging, respectively. A lower AHC content (corresponding to R = 2) and a longer aging time of 2 d yield a binary Y/Eu ceramic with a relatively high transparency; in particular, as the transparency is higher than 80 % in the 1600–2000 nm region, the sample would be suitable for near-infrared applications.

The bandgap energy can be calculated from the transmittance curve using the following equations [37]:

$$\alpha = \frac{1}{d} \ln\left(\frac{1}{T}\right) \quad (4)$$

$$\alpha h\nu = B(h\nu - E_g)^{1/2} \quad (5)$$

where a is the absorption coefficient, d is the sample thickness, T is the transmittance, $h\nu$ is the incident photon energy, B is the absorption constant, and E_g is the bandgap energy.

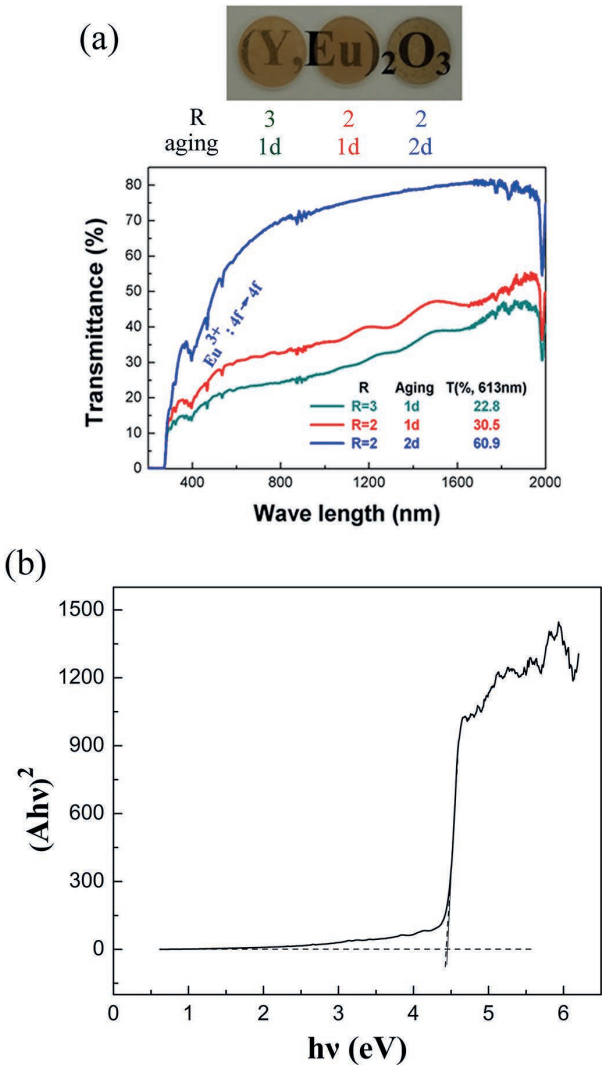

Fig. 4: Appearance (upper part) and in-line transmittance (lower part) of the vacuum-sintered transparent $(Y_{0.95}Eu_{0.05})_2O_3$ ceramics at 1700 °C (a). Plot of $h\nu$ vs. $(Ah\nu)^2$ obtained from the in-line transmittance curve of the ceramic (b).

Fig. 4b shows the $(Ah\nu)^2$ vs. $h\nu$ plot (where A is the absorbance) obtained from the in-line transmittance curve of the ceramic. By extrapolating the linear part of the curve to the x-axis ($y = 0$), the bandgap energy of the ceramic can be estimated to be ~ 4.45 eV, which is much lower than that previously obtained for the Y_2O_3 powder (5.57 eV) [21], owing to a decrease in the centroid energy of the 5*d* orbital of RE^{3+} ions, along with the grain growth of the sintered body.

Fig. 5 displays the microstructures of the thermally etched ceramics and their frequency plots of the dihedral angles. The three ceramic samples with $R = 3$ and 1 d aging, $R = 2$ and 1 d aging, and $R = 2$ and 2 d aging have fine grain sizes of ~ 14, 12, and 12 μm (Figs. 5a-c), respectively. Tiny residual pores are occasionally observed in the dense ceramics, and the three ceramics have corresponding densities of ~ 5.09, 5.11 and 5.16 g/cm^3. The theoretical density of the $(Y_{0.95}Eu_{0.05})_2O_3$ oxide was reported to be ~ 5.16 g/cm^3 [18], and thus their relative densities of the three ceramics are ~ 98.6, 99.0 and 100.0 %, respectively. The relationship among grain boundary energy (γ_b), dihedral angle (θ), and surface energy (γ_s) is given by $\gamma_b = 2\gamma_s cos\theta$; [38] hence, the dispersion of θ has a direct effect on the driving force for densification [39]. The ceramic fabricated under optimal conditions ($R = 2$ and 2 d aging) possesses a rather narrower θ dispersion concentrated in the range 120 – 140° (Fig. 5f) than the others (Figs. 5d and e), denoting a more homogeneous microstructure achieved via uniform densification, and thus exhibits the highest transmittance.

Fig. 6a shows the light intensity output of the as-sintered ceramics using a commercial $CdWO_4$ single crystal as a reference material. The $CdWO_4$ single crystal has an absolute light intensity output of ~ 1400 under an X-ray tube voltage of 90 kV and a current of 2 mA. The samples made

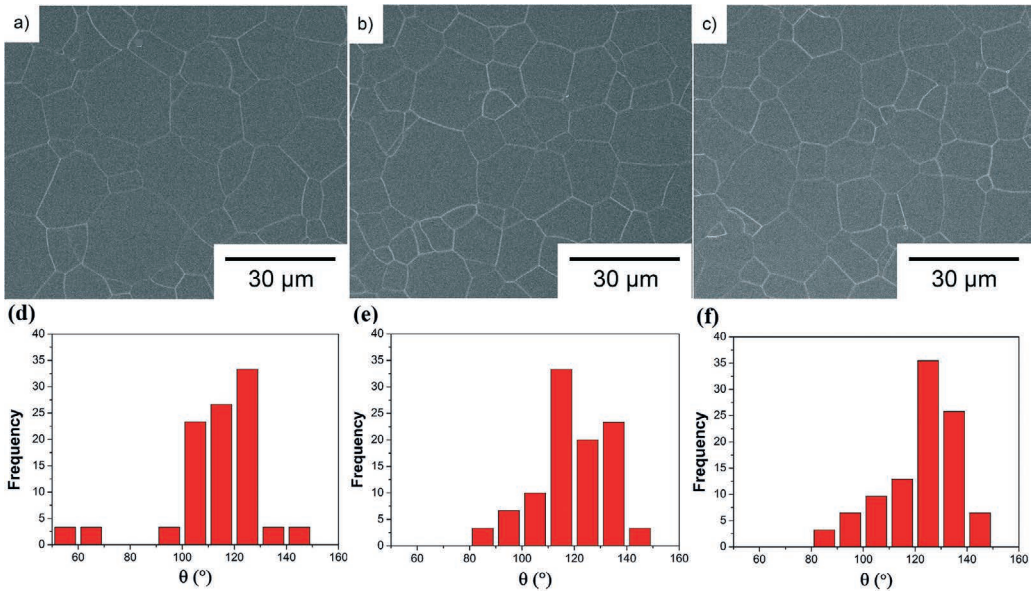

Fig. 5: FE-SEM micrographs displaying the microstructures of the $(Y_{0.95}Eu_{0.05})_2O_3$ ceramics obtained from the precursors prepared with R = 3 and 1 d aging (a), $R = 2$ and 1 d aging (b), and $R = 2$ and 2 d aging (c). Frequency plots of their respective dihedral angles are shown in panels (d) – (f).

from the precursors prepared at $R = 3$ with 1 d aging, $R = 2$ with 1 d aging, and $R = 2$ with 2 d aging exhibit absolute light intensity outputs of ~2100, 1950 and 900, and hence their relative light outputs are ~150, 140, and 64 % of the output corresponding to the $CdWO_4$ single crystal, respectively. After being annealed, the three corresponding ceramics show significantly improved outputs, up to ~200, 200, and 164 % higher, respectively, than the output of the commercial $CdWO_4$ single crystal (Fig. 6b). Such a marked enhancement in light output can be attributed to the effective removal of the oxygen vacancies in the polycrystals.

Photoluminescence (PL) and photoluminescence excitation (PLE) spectra of the $(Y_{0.95}Eu_{0.05})_2O_3$ phosphor powder, as-sintered ceramic, and annealed specimens are shown in Fig. 7a. All samples exhibit the typical red emissions of Eu^{3+} ions driven by the $^5D_0 \rightarrow {}^7F_J$ ($J = 0-4$) transitions, as indicated in the figure. The strongest emission peak at the wavelength of ~613 nm is obtained upon excitation into the CT band arising from the electronic transition from the 2*p* orbital of O^{2-} to the 4*f* orbital of Eu^{3+} (Fig. 7b). The three groups of excitation peaks beyond 290 nm are ascribed to the intra-$4f^6$ electronic transitions of Eu^{3+} [18]. A red shift of up to 20 nm of the CT band center was clearly observed going from the phosphor powder (~252 nm) to the bulk (~272 nm), owing to the smaller surface/grain-boundary area and larger grain size of the sintered body. The as-sintered ceramic possesses much stronger PL and PLE intensities than the powder form, owing to a significantly reduced nonradiative relaxation after high-temperature sintering, while the heat-treated bulk material exhibits further improved PL and PLE intensities (~1.5 times higher than those of the phosphor powder), owing to its higher crystal perfection (i.e. significantly improved crystallinity).

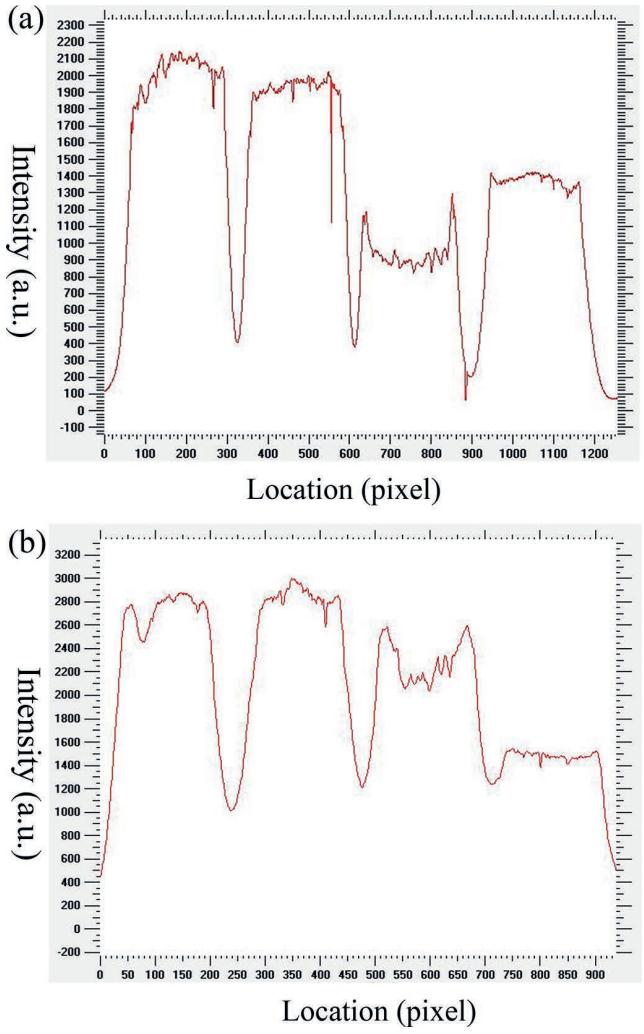

Fig. 6: Light intensity outputs of the as-sintered ceramics (a) and of the corresponding annealed samples (b). The four peaks in each panel from left to right correspond to the ceramics obtained from the precursors synthesized at $R = 3$ with 1 d aging, $R = 2$ with 1 d aging, and $R = 2$ with 2 d aging, and from a commercial $CdWO_4$ single crystal, respectively.

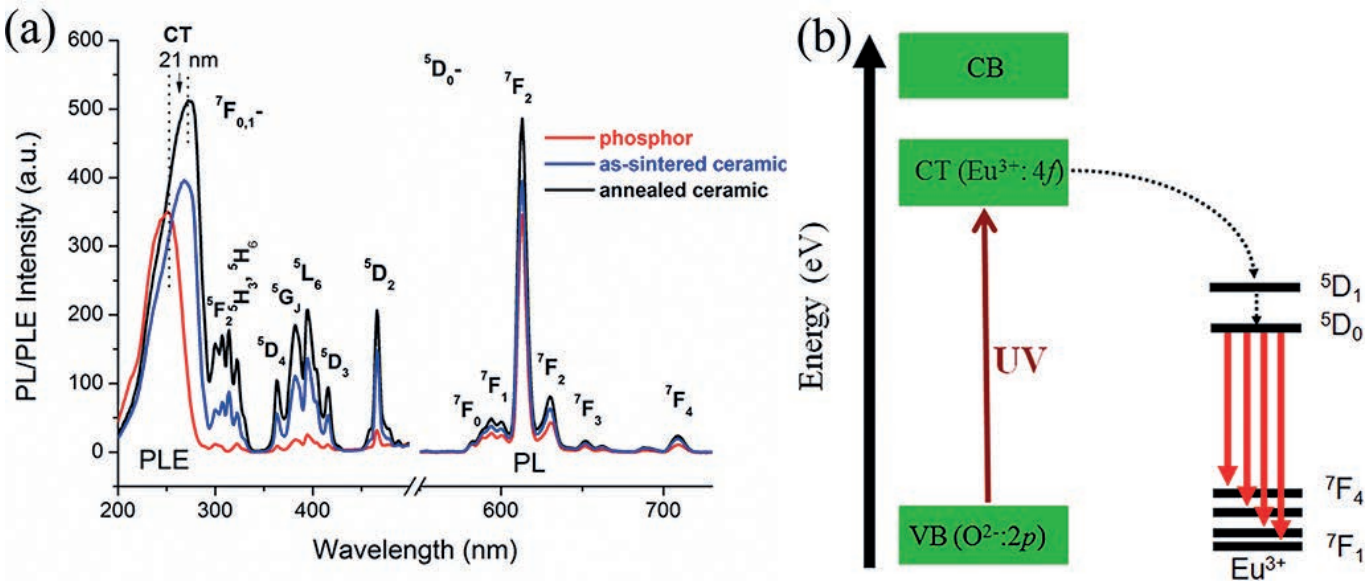

Fig. 7: PL/PLE spectra of the $(Y_{0.95}Eu_{0.05})_2O_3$ phosphor, as-sintered ceramic, and annealed ceramic (a), and energy levels scheme representing the Eu^{3+} emission process upon excitation into the CT band (b).

The fluorescence decay behavior of the 613 nm emission under excitation with the peak wavelength of the CT band is shown in Fig. 8. The fluorescence lifetime can be calculated by fitting the decay curve with the single exponential equation $I = Aexp(-t/\tau) + B$, where I is the emission intensity, τ is the fluorescence lifetime, t is the decay time, and A and B are constants. The fitting procedure yields much shorter lifetimes for the two bulk samples (1.28 ± 0.01 ms for the as-sintered ceramic and 1.17 ± 0.01 ms for the annealed one) than the phosphor powder (2.39 ± 0.01 ms). Eu^{3+} can occupy two crystallographic positions in the C-type cubic RE_2O_3 lattice, namely, a non-centrosymmetric C_2 and a centrosymmetric S_6 (C_{3i}) site. However, the Eu^{3+} ion is preferentially trapped at the C_2 site in the bulk material, which would lead to a much shorter fluorescence lifetime than the S_6 site [40]. On the other hand, the annealed ceramic has a much shorter fluorescence lifetime than the as-sintered one, owing to a further decrease in the defect density. The external quantum efficiencies of the phosphor powder, as-sintered ceramic, and annealed sample are ~55.0, 69.1, and 77.5 %, respectively, since elevated temperatures and subsequent heat treatments further improve the crystallinity of the samples. Such high external quantum efficiency would make the annealed ceramic suitable for various optical applications.

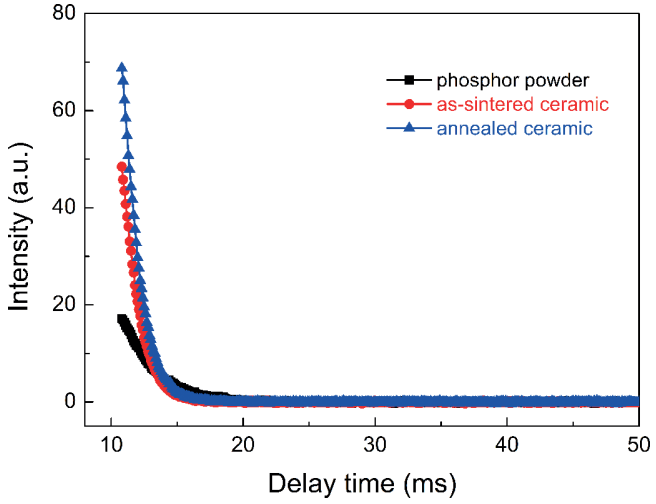

Fig. 8: Fluorescence decay behaviors of the $(Y_{0.95}Eu_{0.05})_2O_3$ phosphor, as-sintered ceramic, and annealed ceramic for the 613 nm Eu^{3+} emission.

IV. Conclusions

Y_2O_3:Eu phosphors were synthesized by means of a co-precipitation route using AHC as the precipitant, whereas transparent Y_2O_3:Eu ceramics were fabricated by vacuum sintering. The R parameter plays an important role in the morphology of the precursors and oxide powders, leading to different transmittances of the obtained ceramics. Both the oxide phosphor and transparent ceramic exhibit characteristic red Eu^{3+} emissions at the wavelength of ~613 nm upon UV excitation into the CT bands at 252–272 nm. The PL/PLE intensities, outputs, and external quantum efficiencies of the ceramics could be further improved via heat treatment. A red shift in the CT band center of the phosphor powder was observed after densification into a transparent ceramic. The lifetime of the bulk ceramic was much shorter than that of the fluorescent powder.

Acknowledgments

The work is supported in part by the National Natural Science Foundation of China (Grant No. 51702171), the Zhejiang Provincial Natural Science Foundation of China (Grant No. LY17E020002), the Zhejiang Provincial Qianjiang Talent Program of China in 2017, and the Ningbo Natural Science Foundation of China (Grant No. 2017A610011). This work was also sponsored by K.C. Wong Magna Fund in Ningbo University.

References

1 Som, S., Das, S., Dutta, S., Visser, H.G., Pandey, M.K., Kumar, P., Dubey, R.K., Sharma, S.K.: Synthesis of strong red emitting $Y_2O_3:Eu^{3+}$ phosphor by potential chemical routes: comparative investigations on the structural evolutions, photometric properties and Judd-Ofelt analysis, *RSC Adv.*, **5**, 70887–70898, (2015).

2 Ferrari, J.L., Cebim, M.A., Pires, A.M., Couto dos Santos, M.A., Savolos, M.R.: $Y_2O_3:Eu^{3+}$ (5 mol%) with Ag nanoparticles prepared by citrate precursor, *J. Solid State Chem.*, **183**, 2110–2115, (2010).

3 Yoo, H.S., Jang, H.S., Im, W.B., Kang, J.H., Jeon, D.Y.: Particle size control of a monodisperse spherical $Y_2O_3:Eu^{3+}$ phosphor and its photoluminescence properties, *J. Mater. Res.*, **22**, 2017–2024, (2007).

4 Adam, J., Metzger, W., Koch, M., Rogin, P., Coenen, T., Atchison, J.S., Konig, P.: Light emission intensities of luminescent Y_2O_3:Eu and Gd_2O_3:Eu particles of various sizes, *Nanomaterials*, **7**, 26, (2017).

5 Wakefield, G., Holland, E., Dobson, P.J., Hutchison, J.L.: Luminescence properties of nanocrystalline Y_2O_3:Eu, *Adv. Mater.*, **13**, 1557–1560, (2001).

6 Byeon, S.H., Ko, M.-G., Park, J.-C., Kim, D.K.: Low-temperature crystallization and highly enhanced photoluminescence of $Gd_{2-x}Y_xO_3:Eu^{3+}$ by Li doping, *Chem. Mater.*, **14**, 603–608, (2002).

7 Lu, B., Li, J.-G., Sun, X.D., Sakka, Y.: Fabrication and characterization of transparent $(Y_{0.98-x}Tb_{0.02}Eu_x)_2O_3$ ceramics with color-tailorable emission, *J. Am. Ceram. Soc.*, **98**, 3877–3883, (2015).

8 Poma, P.Y., Kumar, K.U., Vermelho, M.V.D., Serivalsatit, K., Roberts, S.A., Kucera, C.J., Ballato, J., Jacobsohn, L.G., Jacinto, C.: Luminescence and thermal lensing characterization of singly Eu^{3+} and Tm^{3+} doped Y_2O_3 transparent ceramics, *J. Lumin.*, **161**, 306–312, (2015).

9 Nishiura, S., Tanabe, S., Fujioka, K., Fujimoto, Y.: Properties of transparent Ce:YAG ceramic phosphors for white LED, *Opt. Mater.*, **33**, 688–691, (2011).

10 Lu, S.Z., Yang, Q.H., Wang, Y.G., Li, Y.H., Huang, D.D.: Luminescent properties of Eu:$Y_{1.8}La_{0.2}O_3$ transparent ceramics for potential white LED applications, *Opt. Mater.*, **35**, 718–721, (2013).

11 Lamiri, L., Guerbous, L., Samah, M., Boukerika, A., Ouhenia, S.: Structural, morphological and steady state photoluminescence spectroscopy studies of red Eu^{3+}-doped Y_2O_3 nanophosphors prepared by the sol-gel method, *Lumin.*, **30**, 1336–1343, (2015).

12 Boukerika, A., Guerbous, L.: Annealing effects on structural and luminescence properties of red Eu^{3+}-doped Y_2O_3 nanophosphors prepared by sol-gel method, *J. Lumin.*, **145**, 148–153, (2014).

13 Dhak, P., Patel, S.K.S., Kim, M.-K., Lee, J.-H., Kim, M., Kim, S.K.: Hydrothermal synthesis, structural analysis and

room-temperature ferromagnetism of Y_2O_3:Co^{2+} nanorods, *J. Magn. Magn. Mater.*, **408**, 67 – 72, (2016).

14 Wang, H.B., Qian, C., Yi, Z.G., Rao, L., Liu, H.R., Zeng, S.J.: Hydrothermal synthesis and tunable multicolor upconversion emission of cubic phase Y_2O_3 nanoparticles, *Adv. Cond. Mat. Phys.*, **2013**, 347406, (2013).

15 Gao, L.H., Wang, G.F., Zhu, H.L., Zhou, W.J., Ou, G.F.: Hydrothermal synthesis of Y_2O_3 coated Y_2O_3:Eu^{3+} nanotubes for enhanced photoluminescence properties, *Mater. Res. Bull.*, **70**, 876 – 880, (2015).

16 Li, S.S., Liu, B.L., Li, J., Zhu, X.W., Liu, W.B., Pan, Y.B., Guo, J.K.: Synthesis of yttria nano-powders by the precipitation method: The influence of ammonium hydrogen carbonate to metal ions molar ratio and ammonium sulfate addition, *J. Alloy. Compd.*, **678**, 258 – 266, (2016).

17 Saravanan, T., Raj, S.G., Chandar, N.R.K., Jayavell, R.: Synthesis, optical and electrochemical properties of Y_2O_3 nanoparticles prepared by co-precipitation method, *J. Nanosci. Nanotechnol.*, **15**, 4353 – 4357, (2015).

18 Lu, B., Li, J.-G., Sakka, Y.: Controlled processing of $(Gd,Ln)_2O_3$:Eu (Ln=Y, Lu) red phosphor particles and compositional effects on photoluminescence, *Sci. Technol. Adv. Mater.*, **14**, 064202, (2013).

19 Wang, N.L., Zhang, X.Y., Bai, Z.H., Liu, Q.S., Lu, L.P., Mi, X.Y., Sun, H.Y., Wang, X.C.: Carbonate-precipitation synthesis of Yb^{3+}:Y_2O_3 nanopowders and its characteristics, *Powder Technol.*, **203**, 458 – 461, (2010).

20 Zhu, Q., Li, J.-G., Li, X.D., Sun, X.D.: Effects of Y^{3+} doping on phase structure and photoluminescence properties of $(Gd_{0.95-x}Y_xEu_{0.05})_2O_3$ red phosphors, *Sci. Technol. Adv. Mater.*, **12**, 055001, (2011).

21 Li, J.-G., Li, X.D., Sun, X.D., Ikegami, T., Ishigaki, T.: Uniform colloidal spheres for $(Y_{1-x}Gd_x)_2O_3$ (x=0 – 1): Formation mechanism, compositional impacts, and physicochemical properties of the oxides, *Chem. Mater.*, **20**, 2274 – 2281, (2008).

22 Li, J.-G., Li, X.D., Sun, X.D., Ishigaki, T.: Monodispersed colloidal spheres for uniform Y_2O_3:Eu^{3+} red-phosphor particles and greatly enhanced luminescence by simultaneous Gd^{3+} doping, *J. Phys. Chem. C*, **112**, 11707 – 11716, (2008).

23 Song, L., Li, J.W., Zhang, M., Zhang, B.H., Wang, J.X., Li, Z.H.: Fabrication of Y_2O_3 microspheres by homogeneous precipitation method, *Micro Nano Lett.*, **12**, 241 – 216, (2017).

24 Chen, W.F., Zhou, M.P., Liu, Y., Fu, S.L., Liu, Y., Wang, Y.P., Li, Z.Z., Li, Y.X., Li, Y.Y., Yu, L.X.: Uniform octahedral-shaped Y_2O_3:Eu^{3+} submicron single crystals: Solid-state synthesis, formation mechanism and photoluminescence property, *J. Alloy. Compd.*, **656**, 764 – 770, (2016).

25 Chen, X.D., Liu, N.A., Mei, G.J., Yu, M.M.: Recycling Y and eu from waste fluorescent powder and high temperature solid-state synthesis of Y_2O_3:Eu phosphors, *Minerals*, **7**, 44, (2017).

26 Al-Mamun, S.A., Ishigaki, T.: Influence of hydrogen peroxide addition on photoluminescence of Y_2O_3:Eu^{3+} nanophosphors prepared by laser ablation in water, *J. Am. Ceram. Soc.*, **97**, 1083 – 1090, (2014).

27 Cai, S., Lu, B., Chen, H.B., Pan, J.G., Chen, P.: Homogeneous $(Lu_{1-x}In_x)_2O_3$ (x=0 – 1) solid solutions: Controlled synthesis, structure features and optical properties, *Powder Technol.*, **317**, 224 – 229, (2017).

28 Li, W.J., Zhou, S.M., Liu, N., Lin, H., Teng, H., Li, Y.K., Hou, X.R., Jia, T.T.: Synthesis and spectral properties of Yb^{3+}/Ho^{3+} co-doped yttria 2 μm transparent ceramics, *Mater. Lett.*, **64**, 1344 – 1346, (2010).

29 Huang, Z., Guo, W., Liu, Y., Huang, Q.F., Tang, F., Cao, Y.G.: Synthesis of Nd:Y_2O_3 nanopowders leading to transparent ceramics, *Mater. Chem. Phys.*, **128**, 44 – 49, (2011).

30 Lu, B., Wang, Y., Sun, X.D., Sun, T.: Synthesis of Sc_2O_3 nanopowders and fabrication of transparent, two-step sintered Sc_2O_3 ceramics, *Adv. Appl. Ceram.*, **111**, 389 – 392, (2012).

31 Wang, Y., Lu, B., Sun, X.D., Sun, T., Xu, H.: Synthesis of nanocrystalline Sc_2O_3 powder and fabrication of transparent Sc_2O_3 ceramics, *Adv. Appl. Ceram.*, **110**, 95 – 98, (2011).

32 Ganjkhanlou, Y., Kazemzad, M., Hessari, F.A.: Chromaticity dependence on eu concentration in Y_2O_3:Eu nanopowders, *Nano*, **5**, 111 – 116, (2010).

33 Lu, B., Li, J.-G., Suzuki, TS., Estili, M., Liu, W.G., Sun, X.D., Sakka, Y.: Controlled synthesis of layered rare-earth hydroxide nanosheets leading to highly transparent $(Y_{0.95}Eu_{0.05})_2O_3$ ceramics, *J. Am. Ceram. Soc.*, **98**, 1413 – 1422, (2015).

34 Lu, B., Li, J.-G., Suzuki, T.S., Tanaka, H., Sun, X.D., Sakka, Y.: Effects of gd substitution on sintering and optical properties of highly transparent $(Y_{0.95-x}Gd_xEu_{0.05})_2O_3$ ceramics, *J. Am. Ceram. Soc.*, **98**, 2480 – 2487, (2015).

35 Panchula, M.L., Akinc, M.: Morphology of lanthanum carbonate particles prepared by homogeneous precipitation, *J. Eur. Ceram. Soc.*, **16**, 833 – 841, (1996).

36 Zhang, P., Navrotsky, A., Guo, B., Kennedy, I., Clark, A.N., Lesher, C., Liu, Q.Y.: Energetics of cubic and monoclinic yttrium oxide polymorphs: Phase transitions, surface enthalpies, and stability at the nanoscale, *J. Phys. Chem. C*, **112**, 932 – 938, (2008).

37 Hagfeldt, A., Gratzel, M.: Light-induced redox reactions in nanocrystalline systems, *Chem. Rev.*, **95**, 49 – 68, (1995).

38 Achutaramayya, G., Scott W.: Measurement of dihedral angles by scanning electron microscopy, *J. Am. Ceram. Soc.*, **56**, 230 – 231, (1973).

39 Ikegami, T., Kotani, K., Eguchi, K.: Some roles of MgO and TiO_2 in densification of a sinterable alumina, *J. Am. Ceram. Soc.*, **70**, 885 – 890, (1987).

40 Concas, G., Spano, G., Zych, E., Trojan-Piegza, J.: Nano- and microcrystalline Lu_2O_3:Eu phosphors: variations in occupancy of C_2 and S_6 sites by Eu^{3+} ions, *J. Phys.: Condens. Matter*, **17**, 2594 – 2604, (2005).